Energy Storage Materials 17 (2019) 70–77

Contents lists available at ScienceDirect

Energy Storage Materials

journal homepage: www.elsevier.com/locate/ensm

Synthesis and understanding of $Na_{11}Sn_2PSe_{12}$ with enhanced ionic conductivity for all-solid-state Na-ion battery

Zhaoxin Yu[a], Shun-Li Shang[b], Daiwei Wang[a], Yuguang C. Li[c], Hemant P. Yennawar[c], Guoxing Li[a], Haw-Tyng Huang[b], Yue Gao[c], Thomas E. Mallouk[c], Zi-Kui Liu[b,*], Donghai Wang[a,*]

[a] Department of Mechanical and Nuclear Engineering, The Pennsylvania State University, University Park, PA 16802, United States
[b] Department of Materials Science and Engineering, The Pennsylvania State University, University Park, PA 16802, United States
[c] Department of Chemistry, The Pennsylvania State University, University Park, PA 16802, United States

ARTICLE INFO

Keywords:
Solid-state electrolytes
Sodium-ion batteries
Single crystal X-ray
Selenides
Density functional theory

ABSTRACT

All-solid-state Na-ion batteries (NIBs) that incorporate nonflammable solid-state electrolytes and an inexhaustible alkali metal offer a potential solution to the safety and cost concerns associated with conventional Li-ion batteries that use liquid electrolytes. Na-ion solid-state electrolytes (SSEs) with high ionic conductivity are the key to success for all-solid-state NIBs. Here, we report a new Na-ion SSE, $Na_{11}Sn_2PSe_{12}$, with a superior grain conductivity of 3.04 mS cm^{-1} and a total ionic conductivity of 2.15 mS cm^{-1} at 25 °C. Single-crystal X-ray diffraction, first-principles phonon calculations, and the proposed bonding energy model indicate that its superior ionic conductivity stems from the presence of a high density of dispersive Na^+ vacancies, three-dimensional Na-ion conduction pathways, and a low bonding energy of the Na^+ ion with its neighboring atoms. $Na_{11}Sn_2PSe_{12}$ is used for the first time as the electrolyte in all-solid-state Na-Sn/TiS_2 battery cell, which shows excellent rate performance and delivers a high reversible capacity of 66.2 mAh (g of TiS_2)$^{-1}$ after 100 cycles with cycling retention of 88.3% at a rate of 0.1 C at room temperature.

1. Introduction

Rechargeable Na-ion batteries (NIBs) offer a major cost advantage for large-scale stationary energy storage owing to the wide distribution and abundance of Na sources [1–8]. The development of room-temperature NIBs enabled by nonflammable solid-state electrolytes (SSEs) has attracted much attention because of the potential gains in safety and energy density that could be realized by eliminating liquid electrolytes and optimizing battery fabrication [9–14]. Among Na-ion SSEs, a few solid-state Na-ion oxide conductors (e.g., beta"-Al_2O_3, NASICON, and antiperovskite) have been identified for use in Na-S batteries [15,16]. Sulfide-based Na-ion conductors are also promising electrolytes for all-solid-state NIBs because of their mechanical softness, low grain boundary resistance, and high ionic conductivity at room temperature [17–23].

The development of sulfide-based Na-ion solid-state conductors was investigated in 1980s for Na_2S-GeS_2, Na_2S-SiS_2, and Na_2S-P_2S_5 systems [24,25], which have relatively low conductivities (i.e., < 0.02 mS cm^{-1}) at room temperature [26]. The recent discovery of Na_3PS_4 with a high room-temperature ionic conductivity (σ_{Na}) of 0.2 mS cm^{-1} and its successful application in room-temperature all-solid-state NIBs has stimulated the exploration of sulfide-based Na-ion SSEs [27,28]. Extensive research has been done to increase the conductivity of Na_3PS_4 through either isovalent-ion or aliovalent-ion substitution [29–31]. For example, isovalent substitution of Sb^{5+} for P^{5+} or Se^{2-} for S^{2-} in Na_3PS_4 has led to an ionic conductivity σ_{Na} > 1 mS cm^{-1} [10,32–35]. In the cases of aliovalent-ion substitution, halide doping (F^-, Cl^-, Br^-, and I^-) on the S^{2-} site increases the ionic conductivity by generating Na^+ vacancies, and σ_{Na} = 1.14 mS cm^{-1} was achieved for $Na_{2.9375}PS_{3.9375}Cl_{0.0625}$ at 25 °C [36,37]. In our recent work, aliovalent cation substitution of Sn^{4+} for P^{5+} in Na_3PS_4 resulted in the discovery of a new phase, $Na_{11}Sn_2PS_{12}$ (composition from single-crystal structure analysis: $Na_{10.8}Sn_{1.9}PS_{11.8}$), with σ_{Na} = 0.67 mS cm^{-1} at 25 °C [38]. Similar results have been also reported for $Na_{11}Sn_2PS_{12}$ (composition from single-crystal structure analysis: $Na_{10.78}Sn_2PS_{12}$) with σ_{Na} = 1.4 mS cm^{-1} at 25 °C and $Na_{3.75}Sn_{0.75}Sb_{0.25}S_4$ with σ_{Na} = 0.51 mS cm^{-1} at 30 °C [39,40]. Despite great efforts to develop advanced sulfide-based Na-ion SSEs, ionic conductivities in the current Na-ion sulfides are generally low (< 2 mS cm^{-1}), and there remains a need for Na-ion SSEs with higher ionic conductivities in order to fabricate high-performance room-temperature solid-state Na-ion batteries. Further, while lowering the activation energy and increasing the diffusion pre-factor follow general guidelines for improvement based on the Arrhenius

* Corresponding authors.
E-mail addresses: dr.liu@psu.edu (Z.-K. Liu), dwang@psu.edu (D. Wang).

https://doi.org/10.1016/j.ensm.2018.11.027
Received 29 September 2018; Received in revised form 19 November 2018; Accepted 26 November 2018
Available online 27 November 2018

equation [17,34], there is still a lack of fundamental understanding of how activation energy and diffusion pre-factors can be correlated with atomic-level chemical and physical properties of the sulfide-based Na-ion conductors.

Here we report a new Na-ion solid-state conductor $Na_{11}Sn_2PSe_{12}$ that exhibits a superior grain conductivity of 3.04 mS cm^{-1} and a total ionic conductivity of 2.15 mS cm^{-1} at 25 °C, which is among the highest reported for Na-ion conductors. Notably, the total ionic conductivity of $Na_{11}Sn_2PSe_{12}$ is about 2–3 times higher than that of $Na_{11}Sn_2PS_{12}$. A similar electrolyte but with an nonstoichiometric composition of $Na_{11.1}Sn_{2.1}P_{0.9}Se_{12}$ was reported with a total ionic conductivity of 1.7 mS cm^{-1} at 25 °C during our manuscript preparation, attributing this high ionic conductivity to a lower lattice rigidity and to a weaker Na–chalcogen interaction as compared to $Na_{11}Sn_2PS_{12}$ [41]. However, on the basis of a bonding energy model as well as density functional theory (DFT) based first-principles, phonon, and *ab initio* molecular dynamics (AIMD) calculations, we attribute the enhanced conductivity in $Na_{11}Sn_2PSe_{12}$ to the lower bonding energy of Na^+ ion with its neighboring atoms and the increased disorder of Na^+ ions/vacancies in $Na_{11}Sn_2PSe_{12}$ relative to $Na_{11}Sn_2PS_{12}$. Furthermore, $Na_{11}Sn_2PSe_{12}$ was first examined as the SSE in all-solid-state battery cell containing Na-Sn and TiS_2 electrodes. The increased conductivity of $Na_{11}Sn_2PSe_{12}$ enables excellent rate performance in the cell, and also shows a high reversible capacity of 66.2 mAh (g of TiS_2)$^{-1}$ after 100 cycles and a capacity retention of 88.3% at a rate of 0.1 C at room temperature.

2. Experimental section

2.1. Synthesis

$Na_{11}Sn_2PSe_{12}$ was prepared by heating stoichiometric amounts of Na_2Se (99.5%, Alfa Aesar), phosphorus lump (Alfa Aesar, 99.999%), Sn (Alfa Aesar, 99.995%), and Se (Sigma Aldrich, 99.998%) in an evacuated quartz tube to 900 °C at a rate of 0.5 °C/min, and holding it at 900 °C for 48 hours before cooling to room temperature at a rate of 0.1 °C/min. Brown $Na_{11}Sn_2PSe_{12}$ single crystals were picked out for structural analysis.

2.2. Single crystal X-ray diffraction

X-ray data were collected on a Bruker SMART APEX diffractometer equipped with a fine focus Mo X-ray tube (1600 kW, detector at 5.8 cm, φ and ω scans) at 298 K. SMART (Bruker, 2001) software programs were used for data collection; SAINT (Bruker, 2001) for cell refinement; SAINT and SADABS for data reduction; and OLEX2 for solving and refining the structure. Further details of the crystal structure investigations could be obtained from the Fachinformationszentrum Karlsruhe, 76344 Eggenstein-Leopoldshafen (Germany), on quoting the depository number CSD-434330.

2.3. Characterization of solid electrolytes

Powder X-ray diffraction data were collected on a PANalytical X'Pert Pro MPD θ-θ diffractometer using Cu-Kα radiation at 45 kV and 40 mA. The data were collected over a range of 2θ = 10–70° using fixed slits (0.125° PDS and 0.25° FAS) and 0.04 rad Soller slits in conjunction with a polycarbonate domed sample holder and an anti-scatter slit for transmission geometry in front of a PIXcel 1D detector. The detector was operated in scanning line mode with an active length of 3.347°. Rietveld refinement was performed using the Materials Studio 8.0. DSC experiments were conducted on $Na_{11}Sn_2PSe_{12}$ and $Na_{11}Sn_2PS_{12}$ powders in closed alumina crucibles in a N_2 gas flow using a Q2000 MDSC (Modulated Differential Scanning Calorimeter). The scan rate was 10 °C min^{-1}. For XPS characterization, a pristine $Na_{11}Sn_2PSe_{12}$ sample and a sample that had been contacted with Na metal were loaded in a glovebox filled with Ar gas and transferred into the instrument (*Physical Electronics VersaProbe II*) through a vacuum transfer vessel. The elemental ratio was determined by inductively coupled plasma (ICP-AES, Perkin-Elmer Optima 5300).

2.4. Ionic and electronic conductivities

For ionic conductivity measurements, carbon-coated aluminum foil, as a blocking electrode, was pressed onto both sides of a cold-pressed $Na_{11}Sn_2PSe_{12}$ pellet at a pressure of 400 MPa, and heated at 350 °C under vacuum before measuring the ionic conductivity. The a.c. impedance was measured between −120 °C and 70 °C in the frequency range of 1 MHz to 1 Hz with an amplitude of 5 mV using a Solartron Modulab. The electronic conductivity was measured by the Hebb-Wagner polarization method [42].

2.5. Battery performance characterization

All-solid-state Na-ion batteries were fabricated by pressing Na-Sn alloy foil and TiS_2 power (Sigma-Aldrich, 99.9%) onto two faces of the Na_3PS_4-$Na_{12}Sn_2PSe_{12}$ bilayer pressed pellet. The Na-Sn alloy foil was prepared by pressing Na metal onto the Sn foil with the mole ratio of Na:Sn = 3:4 under the pressure of 400 MPa. The pellet so obtained was assembled into a 2032-type coin cell. These fabrication steps were carried out in an Ar-filled glovebox. The cell was cycled in the voltage range from 1.5 to 2.5 V (vs. Na^+/Na) using a BTS-5V1mA Neware battery test system at room temperature.

2.6. First-principles, phonon, and AIMD calculations

The structure of $Na_{11}Sn_2PSe_{12}$ used in DFT calculations was taken from our previous work, i.e., the Str2 of $Na_{11}Sn_2PS_{12}$ [38]. All DFT-based first-principles, phonon, and AIMD calculations were performed by using the Vienna *Ab initio* Simulation Package (VASP) [43] in terms of four exchange-correlation functionals. Phonon calculations were performed by YPHON code [44] with VASP again as the computational engine. AIMD simulations were performed for $Na_{11}Sn_2PSe_{12}$ using the VASP code in terms of a canonical ensemble at equilibrium volumes at several temperatures. Thermodynamic properties of Na_3PSe_4, Na_4SnSe_4, $Na_{11}Sn_2PSe_{12}$, and LGPS-type $Na_{10}SnP_2Se_{12}$ were determined by the quasiharmonic approach in terms of first-principles and phonon calculations [45]. More details together with first-principles, phonon, and AIMD results are shown in the SI Supplement, including structural properties, stretching force constants, thermodynamic properties, and diffusion coefficients for $Na_{11}Sn_2PSe_{12}$, Na_3PSe_4, Na_4SnSe_4, and $Na_{10}SnP_2Se_{12}$.

3. Results and discussion

3.1. Crystal structure of $Na_{11}Sn_2PSe_{12}$

$Na_{11}Sn_2PSe_{12}$ powder was synthesized by heating the raw materials (Na_2Se, Sn, P, and Se) in a stoichiometric ratio at 900 °C in an evacuated quartz tube (see details in *Experimental* section). The ratio among the four elements was found to be Na:Sn:P:Se = 11.93:2.03:1:12.31 by the inductively coupled plasma (ICP) spectroscopy. The crystal structure of $Na_{11}Sn_2PSe_{12}$ was analyzed by using single-crystal X-ray diffraction (XRD) and powder XRD techniques. Fig. 1A, B shows the crystal structure of $Na_{11}Sn_2PSe_{12}$ as solved by single-crystal XRD at 298 K, with data collection and refinement details summarized in Table S1 (see SI Supplement). The structure was solved in tetragonal space group $I4_1/acd$ (no. 142) (a = 13.252 Å, c = 28.41(3) Å, and Z = 8) and the compound was found to be isostructural with $Na_{11}Sn_2PS_{12}$ [38]. Details of atomic occupancies are summarized in Table S2 (see SI Supplement). Na^+ ions are distributed over six Wyckoff positions in the unit cell, i.e., 16e (Na1 with site occupancy factor (sof) ~ 0.95), 16c (Na2 with sof ~ 0.92), 32 g (Na3 with sof ~ 0.82), 16 f (Na4 with sof ~ 0.90),

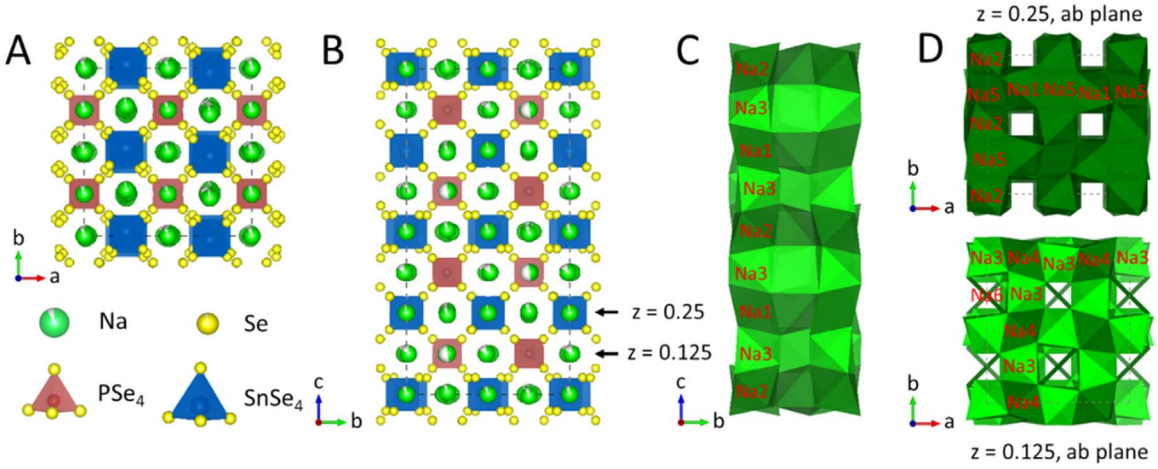

Fig. 1. A-B) Different views of the crystal structure of $Na_{11}Sn_2PSe_{12}$ with white color in the green Na spheres indicating vacancies. C) Illustration of the arrangement of $NaSe_6$ octahedra along the c-axis with the -Na2-Na3-Na1-Na3-Na2-Na3-Na1- chain. D) View of the arrangement of $NaSe_6$ octahedra in the a-b plane. The sites with lower site occupancy factors (Na3 and Na6) are shown in light green, and the sites with higher site occupancy factors (Na1, Na2, and Na5) are dark green. (For interpretation of the references to color in this figure legend, the reader is referred to the web version of this article).

16d (Na5 with sof ~ 0.91), and 8b (Na6 with sof ~ 0.35). These partially occupied positions provide considerable Na^+ vacancies (i.e., 16.1%, see also the sof values in the SI Supplement, Table S2). All of Na^+ ions occupy octahedral sites formed by six Se^{2-} ions (four of them with Na-Se distances $r_{Na\text{-}Se}$ (r_{Se} for short) < 3.1 Å and two of them with 3.1 Å < r_{Se} < 3.5 Å), except for Na6 which sits in an octahedral site that is formed by four Se^{2-} (r_{Se} = 3.46 Å) and two Na-ions (r_{Na} = 3.39 Å). Details of coordination numbers for each kind of Na^+ ion are summarized in the SI Supplement, Table S3. The arrangement of Na^+ ions along the [001], [010], and [100] directions is illustrated in Fig. 1C, D. The $NaSe_6$ octahedra connect with each other by shared faces in all directions to form a three-dimensional (3-D) network. Notably, the second least occupied Na3 site (sof ~ 0.82) is located between the almost fully occupied Na1 (sof ~ 0.95) and Na2 (sof ~ 0.92) sites, forming a -Na2-Na3-Na1- chain along the [001] direction, as shown in Fig. 1C. A similar alternating arrangement of less occupied Na3 sites and highly occupied Na4 sites is also present in the a-b plane with z = 0.125 (Fig. 1D). These Na^+ ion tunnels with a large number of Na^+ vacancies promote vacancy-driven Na^+ ion migration with a superior ionic conductivity in $Na_{11}Sn_2PSe_{12}$. Further analysis using the local interatomic bonding energy model (see Eq. (2) and discussion below) indicates that Na^+ ions in the Na1, Na2, and Na4 sites have higher bonding energies (> 62 eV) with their surrounding atoms, corresponding to higher activation energy and hence lower ionic diffusivity and conductivity, whereas Na^+ ions in the Na3, Na5, and Na6 sites have weaker bonding energies (< 45 eV), corresponding to lower activation energy, and hence higher ionic diffusivity and conductivity. Fig. 2A shows the powder XRD pattern of $Na_{11}Sn_2PSe_{12}$ together with the Rietveld refinement based on the crystal structure obtained from single crystal XRD. The low R-Bragg factor (4.66%) indicates that phase-pure $Na_{11}Sn_2PSe_{12}$ powders were synthesized.

3.2. Ionic and electronic conductivities of $Na_{11}Sn_2PSe_{12}$

To measure the ionic conductivity, $Na_{11}Sn_2PSe_{12}$ powder was pressed into a pellet and sintered at 350 °C for 12 hours. The differential scanning calorimetry (DSC) curve of $Na_{11}Sn_2PSe_{12}$ in Fig. 2B shows no obvious peaks, suggesting that the phase is stable up to 400 °C. In contrast, clear exothermic and endothermic peaks corresponding to phase transitions were observed in the DSC curve of $Na_{11}Sn_2PS_{12}$, indicating relatively poor phase stability with temperature cycling. The $Na_{11}Sn_2PSe_{12}$ pellet was also characterized by electrochemical impedance spectroscopy (EIS) at different temperatures in the range between −120 °C and 70 °C at a step size of 10 °C, as shown in the SI Supplement, Fig. S1. The Nyquist plot of $Na_{11}Sn_2PSe_{12}$ at T = −110 °C, shown in Fig. 2C, includes a semicircle in the high-frequency region (10^6–10^3 Hz), a half semicircle in the intermediate frequency region (10^3–10 Hz), and a spike in the low-frequency region (10–1 Hz), corresponding to contributions from grain, grain boundary, and electrode polarization, respectively. The contributions from each part were analyzed in more detail by fitting the spectrum to the equivalent circuit shown in the inset of Fig. 2C. Here the grain impedance is represented by an ohmic resistance in parallel with a constant phase element (R_g‖CPE_g), the grain boundary impedance by R_{gb}‖CPE_{gb}, and the electrode impedance by CPE_{ep}. Fitting results for spectra obtained at different temperatures are summarized in the SI Supplement, Table S4. The grain conductivity ($\sigma_{Na}{}^g$, calculated as $\sigma_{Na}{}^g = C/R_g$) and the total ionic conductivity ($\sigma_{Na}{}^t$, calculated as $\sigma_{Na}{}^t = C/R_t$) at each temperature were extracted from fits to the equivalent circuit, where C = d/A is the ratio of the pellet thickness (d) to the sample area (A), and the total resistance $R_t = R_g + R_{gb}$. Plots of the grain and total conductivity are shown in Fig. 2D. The grain conductivity, $\sigma_{Na}{}^g$, is Arrhenius-activated with an activation energy of Q^g = 0.28 eV. Extrapolation of the Arrhenius fit for $\sigma_{Na}{}^g$ to T = 298 K indicates a superior grain conductivity of 3.04 mS cm^{-1}. Unlike $\sigma_{Na}{}^g$, the total conductivity $\sigma_{Na}{}^t$ does not show Arrhenius behavior, probably because of the contribution from grain boundary resistance. A similar phenomenon was previously observed for $Li_{10}SnP_2S_{12}$ [46]. The total ionic conductivity of $Na_{11}Sn_2PSe_{12}$ is calculated to be 2.15 mS cm^{-1} at 298 K, which is among the highest reported for Na-ion conductors.

The temperature-dependent ionic conductivity of $Na_{11}Sn_2PSe_{12}$ in comparison with other reported Na-ion SSEs is shown in Fig. 2E. The ionic conductivity of $Na_{11}Sn_2PSe_{12}$ is obviously higher than those of $Na_3P_{0.62}As_{0.38}S_4$ [47], $Na_{3.75}Sn_{0.75}Sb_{0.25}S_4$ [48], and $Na_{11}Sn_2PS_{12}$ [38] within the temperature range between -40 °C to 70 °C, and at least one order of magnitude higher than those of such as the tetragonal Na_3PS_4 [27], $50Na_2S$-$50SiS_2$ [26], $60Na_2S$-$40GeS_2$ [26], and $Na_3Zr_2Si_2PO_{12}$ [49]. Notably, different room-temperature ionic conductivities of $Na_{11}Sn_2PS_{12}$ (0.67 [38], 1.4 [39], and 3.7 mS cm^{-1} [50]) are reported by three different groups. The conductivities of $Na_{11}Sn_2PS_{12}$ in Fig. 2E are from our previous work. It is well-known that the measured ionic conductivity is affected by many experimental conditions, e.g., hot-sintering, pressure for forming electrolyte pellets, and pressure during the measurement [51]. The higher relative density, the less grain boundary resistance, and the higher measured ionic conductivity. Both of high pressure and high temperature (e.g., hot pressing and high-temperature sintering) assist in forming pellets with high relative density. Besides increasing the relative density of the pellet itself,

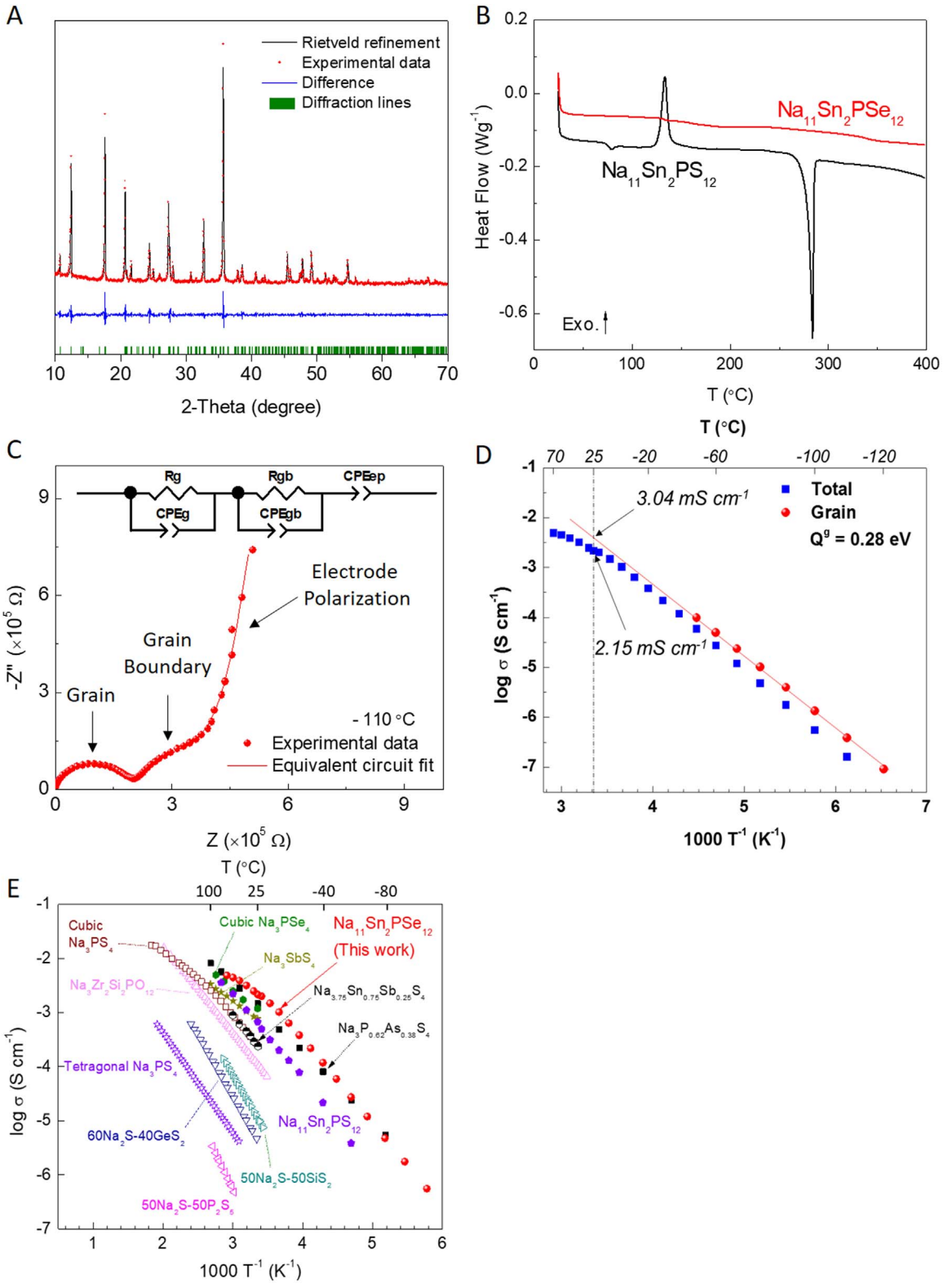

Fig. 2. A) Powder XRD pattern of the as-prepared $Na_{11}Sn_2PSe_{12}$ and Rietveld refinement. Red dots represent the experimental data and black solid line corresponds to the refined pattern. The difference between experimental and refined patterns is shown in blue. The vertical green bars at the bottom indicate the expected positions of Bragg reflections of tetragonal $Na_{11}Sn_2PSe_{12}$. The refined R-Bragg = 4.66%. B) Differential scanning calorimetry curves of $Na_{11}Sn_2PSe_{12}$ and $Na_{11}Sn_2PS_{12}$ at a heating rate of 10 °C min^{-1}. C) Nyquist plot of the impedance for $Na_{11}Sn_2PSe_{12}$ at -110 °C. The corresponding equivalent circuit fit curves are displayed as solid lines. D) Plots of total and grain conductivities of a $Na_{11}Sn_2PSe_{12}$ pellet in the temperature range between −120 °C and 70 °C. E) The temperature-dependent ionic conductivity of $Na_{11}Sn_2PSe_{12}$ in comparison with other reported Na-ion SSEs in the literature.

maintaining good contact between the pellet and electrodes at two sides of the pellet (additional sintering or providing a certain pressure while measuring) is also critical in achieving high measured ionic conductivity [17]. Therefore, different reported ionic conductivities for $Na_{11}Sn_2PS_{12}$ are probably due to different experimental conditions. Although the ionic conductivity of $Na_{11}Sn_2PSe_{12}$ is not higher than that of $Na_{11}Sn_2PS_{12}$ reported by Dehnen's group [50], it is higher than the values reported by our group [38] and Nazar's group [39], indicating that Se-substitution does enhance the ionic conductivity.

The electronic conductivity of $Na_{11}Sn_2PSe_{12}$ was determined by the Hebb-Wagner method using the asymmetric cell (-) Na/$Na_{11}Sn_2PSe_{12}$/Al (+) at 25 °C [42]. The total electronic conductivity (electron + hole) was calculated at the irreversible interface $Na_{11}Sn_2PSe_{12}$/Al by linear fitting between 2 V to 3.5 V (see SI Supplement, Fig. S2). Using $\sigma_{e+h} = (\frac{L}{A})(d|I_{e,h}|/dE)$ (where L is the thickness of the pellet, A the surface area, $I_{e,h}$ the total electronic current, and E the applied voltage), the electronic conductivity was determined to be 1.87×10^{-7} S cm^{-1}. The ratio of Na^+ ionic conductivity (i.e., 2.15 mS cm^{-1}) to the total electronic and ionic conductivity is 0.9999999, indicating that the ion transference number is unity and $Na_{11}Sn_2PSe_{12}$ is a pure ionic conductor.

3.3. Mechanism behind superior ionic conductivity of $Na_{11}Sn_2PSe_{12}$

In general, the ionic conductivity σ of SSEs is governed by an activated hopping process of ions with an activation energy Q and diffusion pre-factor D_0 based on the Arrhenius equation [52,53]:

$$\sigma \propto D = D_0 \exp(-Q/k_B T) \quad (1)$$

where k_B is Boltzmann's constant and T the temperature. Q is mainly determined by the bonding energy between mobile ions and their neighboring atoms, whereas D_0 is related to entropy (see details in the SI Supplement). To understand the superior ionic conductivity in $Na_{11}Sn_2PSe_{12}$ (relative to $Na_{11}Sn_2PS_{12}$), the diffusion activation energy Q — which corresponds to breaking the bonds between the Na^+ ion and its neighboring atoms — was analyzed by DFT calculations, since a lower Q leads to a higher ionic conductivity in a given crystal structure [25]. The effect of entropy on diffusion was also examined in terms of DFT calculations.

Following our successful analysis of Q in $Na_3As_xP_{1-x}S_4$ by examining the Na-S bonding energy [47], we propose that the diffusion activation energy Q can be characterized by a local interatomic bonding energy model,

$$Q \propto \varepsilon = \sum_X \mathrm{sof}_X \bullet m_X \eta_X r_X^2 \quad (2)$$

where ε is total bonding energy for the atom/ion of interest (here, Na^+) determined by interactions with its neighboring atoms X. By considering only the first coordination shells of Na^+, m_X is equal to the coordination number or multiplicity of X. sof_X represents the site occupancy factor of X (this term is usually adopted when measured crystallographic information is available), and η_X represents the stretching force constant between Na and X with a bond length of r_X. Force constants enable quantitative analysis of the extent of interaction or bonding between atomic pairs of interest [54,55]. A large and positive η_X suggests strong interaction (bonding), whereas a negative η_X indicates that the ionic pairs tend to separate from each other. η_X can be predicted by DFT-based phonon calculations [56]. m_X and r_X can be determined by means of the radial distribution function (RDF) around Na (see Supplemental Fig. S4). Note that only the first shell of the RDF for each Na-X is considered due to the rapid decrease of η_X as a function of bond length (see SI Supplement, Fig. S3).

Fig. 3 shows the stretching force constants for Na-X (X = Na, Sn, P, S, and Se) by examining six Na-containing chalcogenides $Na_3P\Theta_4$, $Na_4Sn\Theta_4$, and $Na_{11}Sn_2P\Theta_{12}$ (Θ = S or Se). It shows that the stretching force constant η_X for each Na-X nicely follows a curve even though they are from

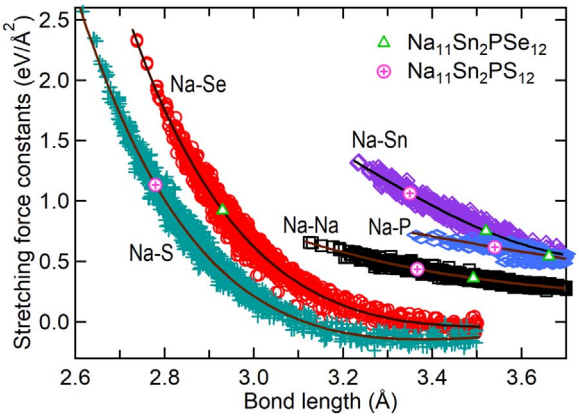

Fig. 3. Stretching force constants of Na^+ with neighboring atoms in the first coordination shell by examining $Na_3P\Theta_4$, $Na_4Sn\Theta_4$, and $Na_{11}Sn_2P\Theta_{12}$ (Θ = S or Se) at several volumes. The symbols Δ and ⊕ indicate the average bond lengths (see their determinations via RDF in the SI Supplement, Fig. S4) and the corresponding stretching force constants in $Na_{11}Sn_2P\Theta_{12}$; see also the r_{peak} and η_X values in Table 1. The other symbols are phonon calculations with the lines showing fits (see SI Supplement, Table S5).

different compounds, suggesting that the force constants are transferable across different compounds (see the fitted results in the SI Supplement, Table S5). Hence, the bonding energy calculated from Eq. (2) is reasonable even for different chalcogenides. From Fig. 3, $Na_{11}Sn_2PSe_{12}$ shows a dramatic decrease in stretching force constants for Na-Sn as well as for Na-Θ relative to their values in $Na_{11}Sn_2PS_{12}$, indicating lower bonding energies for Na-Sn and Na-Se in $Na_{11}Sn_2PSe_{12}$. According to Eq. (2), the average bonding energies between Na^+ ions and their neighboring atoms in the first coordination shell are 73.4 eV in $Na_{11}Sn_2PS_{12}$ and 65.1 eV in $Na_{11}Sn_2PSe_{12}$, respectively. Detailed analyses of Na-X bonding energies using Eq. (2) and DFT calculations are summarized in Table 1, showing that the decrease of bonding energy (8.3 eV) from $Na_{11}Sn_2PS_{12}$ to $Na_{11}Sn_2PSe_{12}$ is mainly from the Na-Se (decrease of 3.6 eV) and Na-Sn bonds (decrease of 3.0 eV). The lower bonding energies (65.1 eV vs. 73.4 eV) agree well with the measured activation energy (0.28 eV for $Na_{11}Sn_2PSe_{12}$ vs. 0.31 eV for $Na_{11}Sn_2PS_{12}$) [38], indicating that the lower activation energy Q can be ascribed mainly to the weaker Na-Se and Na-Sn interactions. Notably, the weaker Na-Se bonding was considered to be the main or even sole reason for the increase in ionic conductivity for samples with Se-substitution/doping [33–35,57,58]. In contrast, our results show that all the interactions between Na^+ ions and their neighboring atoms (especially Na-Sn in $Na_{11}Sn_2PSe_{12}$) contribute to the increased ionic conductivity. The local interatomic bonding energy model should also be applicable to other structural families by considering transferable force constants, serving as a broadly useful guide for designing solid-state conductors and achieving higher ionic conductivity.

The model based on Eq. (2) is also able to predict the diffusivity as

Table 1
Average bonding energy ε of Na with respect to its surrounding atoms (see Eq. (2)) in $Na_{11}Sn_2PS_{12}$ [represented by the symbol (S)] and $Na_{11}Sn_2PSe_{12}$ [represented by the symbol (Se)]. Here, r_{peak} indicates the peak position of the nearest Na-X (X = Na, Sn, P, S, or Se) shell in the RDF profile, see SI Supplement Fig. S4 for the case of $Na_{11}Sn_2PSe_{12}$; and ε_{diff} indicates the bonding energy difference of Na in $Na_{11}Sn_2PSe_{12}$ and $Na_{11}Sn_2PS_{12}$. Note that the stretching force constants η_X are determined by the fitted lines, see Fig. 3 and SI Supplement Table S5. DFT predicted structures by PS+D3 were used to determine m_X and r_{peak}.

Na-X or Total ε	m_X		r_{peak} (Å)		η_X (eV/Å^2)		ε (eV)		ε_{diff} (eV)
	(S)	(Se)	(S)	(Se)	(S)	(Se)	(S)	(Se)	
Na-Na	2.82	2.82	3.37	3.49	0.44	0.36	14.0	12.5	−1.5
Na-Sn	1.09	1.09	3.35	3.52	1.09	0.77	13.3	10.3	−3.0
Na-P	0.45	0.45	3.54	3.66	0.62	0.54	3.5	3.3	−0.2
Na-S/Se	4.77	4.85	2.78	2.93	1.15	0.94	42.6	38.9	−3.6
Total ε							73.4	65.1	−8.3

well as the conductivity of Na^+ ions in the six Wyckoff positions by analyzing their bonding energies with neighboring atoms. The coordination number and the predicted bonding energy for Na^+ ions in each kind of site are given in the SI Supplement, Table S3. In principle, Na^+ ions in both $Na_{11}Sn_2PS_{12}$ and $Na_{11}Sn_2PSe_{12}$ can be categorized into three groups: (i) Na^+ ions with high ε (> 70 eV in $Na_{11}Sn_2PS_{12}$ and > 62 eV in $Na_{11}Sn_2PSe_{12}$) and high sof (> 0.9), for ions located in the Na1, Na2, and Na4 sites. These Na^+ ions possess high bonding energies, and thus low ionic diffusivities and conductivities, which are due mainly to their short bonding distance with S (< 2.81 Å) or Se (< 2.85 Å). (ii) Na^+ ions with lower ε (~ 40 eV in both $Na_{11}Sn_2PS_{12}$ and $Na_{11}Sn_2PSe_{12}$ cases) and lower sof (0.8 < sof < 0.9), which are located in Na3 and Na5 sites. These Na^+ ions possess relatively low bonding energies, and thus higher ionic diffusivities and conductivities, which are due mainly to $m_{Sn} = 0$ (or $\varepsilon_{Sn} = 0$). (iii) Na^+ ions with the lowest ε (30 eV for $Na_{11}Sn_2PS_{12}$ and 25 eV for $Na_{11}Sn_2PSe_{12}$) and the lowest sof (0.12 for $Na_{11}Sn_2PS_{12}$ and 0.35 for $Na_{11}Sn_2PSe_{12}$), which are located in the Na6 site. These Na^+ ions possess the lowest bonding energies and thus the highest ionic diffusivities and conductivities because $m_{Sn} + m_P + m_{S/Se} = 0$ (or $\varepsilon_{Sn} + \varepsilon_P + \varepsilon_{S/Se} = 0$). The SI Supplement, Table S3, shows that the bonding energy of Na^+ ions at each kind of site in $Na_{11}Sn_2PSe_{12}$ is lower than that in $Na_{11}Sn_2PS_{12}$, especially for Na^+ ions in Na1, Na2, and Na4 sites, which show the largest decrease in bonding energy from $Na_{11}Sn_2PS_{12}$ to $Na_{11}Sn_2PSe_{12}$, contributing to higher ionic diffusivity and conductivity in $Na_{11}Sn_2PSe_{12}$.

In addition to the lower Na-X bonding energies in $Na_{11}Sn_2PSe_{12}$, it is interesting to note that the more dispersive distribution of Na^+ vacancies among six kinds of sites in $Na_{11}Sn_2PSe_{12}$ results in a higher configurational entropy S_{conf} than in $Na_{11}Sn_2PS_{12}$ [38]. This results in a higher ionic diffusivity and conductivity based on the theory of Adam and Gibbs [59,60], i.e., $\propto \exp\left(\frac{-C}{TS_{conf}}\right)$, where C is a parameter associated with the Gibbs free energy difference and configurational partition function of the ensemble of subsystems. According to the crystal structure solutions for $Na_{11}Sn_2P\Theta_{12}$ (Θ = S or Se) (see SI Supplement, Table S2), the concentration of Na^+ vacancies is similar in $Na_{11}Sn_2PSe_{12}$ (16.1%) and $Na_{11}Sn_2PS_{12}$ (17%), but Na^+ vacancy is more dispersive across six kinds of sites in $Na_{11}Sn_2PSe_{12}$. Based on the sublattice model (see SI Supplement) for the measured Na positions in $Na_{11}Sn_2PSe_{12}$ and $Na_{11}Sn_2PS_{12}$, the calculated S_{conf} values are $0.169k_B$ and $0.151k_B$ for $Na_{11}Sn_2PSe_{12}$ and $Na_{11}Sn_2PS_{12}$, respectively, indicating a higher configurational entropy for $Na_{11}Sn_2PSe_{12}$.

Our AIMD results (see SI Supplement, Fig. S8) indicate higher diffusion coefficients for $Na_{11}Sn_2PSe_{12}$ relative to $Na_{11}Sn_2PS_{12}$. The activation energies for $Na_{11}Sn_2PSe_{12}$ are in the range of 0.29–0.39 eV based on the fits at selected data points, in reasonable agreement with the experimental measurements (0.28 eV for grain conductivity, Fig. 2D) despite the fact that the AIMD simulations were performed at higher temperature (600–1400 K).

3.4. Electrochemical properties of $Na_{11}Sn_2PSe_{12}$ and all-solid-state battery Na-Sn/Na_3PS_4-$Na_{11}Sn_2PSe_{12}$/TiS_2

In order to determine the electrochemical stability window of $Na_{11}Sn_2PSe_{12}$, cyclic voltammetry (CV) was conducted on the cell Na/$Na_{11}Sn_2PSe_{12}$/Stainless Steel (SS) with Na serving as the counter/reference electrode and SS as the working electrode. From the CV results (see SI Supplement, Fig. S9), a cathodic (reducing) current starting at 1.22 V (vs. Na^+/Na) and an anodic (oxidizing) current starting at 2.65 V were observed, suggesting that the electrochemical stability window of $Na_{11}Sn_2PSe_{12}$ is 1.22–2.65 V (vs. Na^+/Na). Reduced Sn species and Na_2Se were detected as reduction products of $Na_{11}Sn_2PSe_{12}$ against Na from X-ray photoelectron spectroscopy (Supplementary Fig. S10). This is similar to the reaction observed for $Na_{11}Sn_2PS_{12}$ in contact with Na metal [38].

$Na_{11}Sn_2PSe_{12}$ was further examined as the electrolyte in all-solid-state Na-Sn/Na_3PS_4-$Na_{11}Sn_2PSe_{12}$/TiS_2 battery cell, which was cycled between 1.5 V and 2.5 V (vs. Na^+/Na) at 25 °C. Bilayer structure Na_3PS_4-$Na_{11}Sn_2PSe_{12}$ was employed to eliminate any side reactions between the Na-Sn alloy and $Na_{11}Sn_2PSe_{12}$. The current density and specific capacity were calculated based on the mass of TiS_2 in the cathode. Fig. 4A shows voltage profiles in the 2nd and 3rd cycles at a current density of 12 mA g^{-1} (0.05 C), which delivers a reversible specific capacity of 85 mAh g^{-1}. The specific capacity of TiS_2 is relatively low compared to its theoretical value (240 mAh g^{-1}). We believe that the specific capacity could be further enhanced by engineering fabrication of the Na-Sn/Na_3PS_4-$Na_{11}Sn_2PSe_{12}$/TiS_2 pellet with improved interfacial contacts and by optimizing the ratio among TiS_2, the solid electrolyte, and carbon additive. The rate performance of the cell is also shown in Fig. 4B. Even at 1 C, it still delivers a capacity as high as 23 mAh g^{-1}, suggesting remarkable structural stability of $Na_{11}Sn_2PSe_{12}$ and good compatibility between $Na_{11}Sn_2PSe_{12}$ and TiS_2 even at a very high current density (1 C). When the rate is restored to 0.1 C, the specific capacity fully recovers to the original value. This excellent rate performance is attributed mainly to the high ionic conductivity of $Na_{11}Sn_2PSe_{12}$. Notably, the cell also exhibits an outstanding capacity retention of ~ 88.3% in the 100th cycle with respect to the capacity of the 8th cycle (75.3 mAh g^{-1}), highlighting the potential of $Na_{11}Sn_2PSe_{12}$ for practical all-solid-state NIBs.

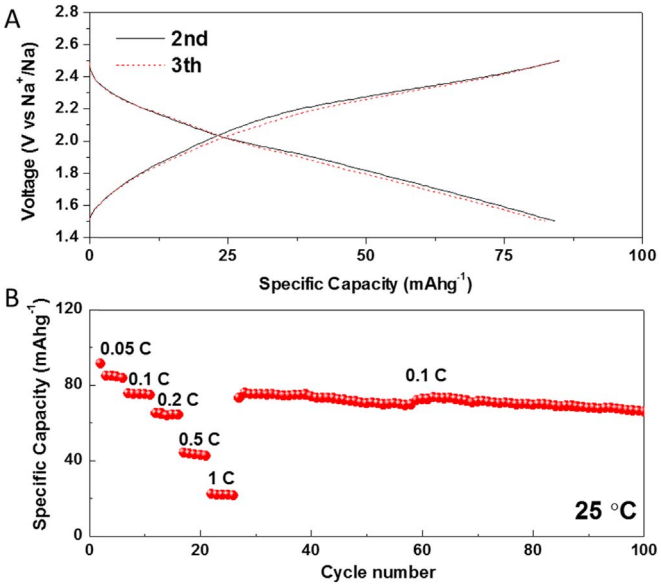

Fig. 4. A) Voltage profiles and B) rate performance of an all-solid-state Na-Sn/Na_3PS_4-$Na_{11}Sn_2PSe_{12}$/TiS_2 battery cell. The cell was cycled between 1.5 and 2.5 V (vs. Na^+/Na) at 25 °C. Here, 1 C = 240 mA g^{-1}, based on the mass of TiS_2.

4. Conclusion

In summary, the Na-ion SSE $Na_{11}Sn_2PSe_{12}$ with the space group of $I4_1/acd$ exhibits a superior grain conductivity of 3.04 mS cm^{-1} and a high total ionic conductivity of 2.15 mS cm^{-1} at 25 °C. Based on experimental results and first-principles, phonon, and AIMD calculations, the local interatomic bonding energy model for diffusion activation barrier is proposed in terms of Eq. (2). It is concluded that the origin of the exceptional conductivity of $Na_{11}Sn_2PSe_{12}$ is due to three factors: (i) 3-D Na-ion conduction pathways, (ii) a large number of Na^+ vacancies and their dispersed distribution in the structure, and (iii) the low bonding energy of Na^+ with neighboring atoms (especially Na-Se and Na-Sn). The all-solid-state Na-Sn/TiS_2 battery cell with $Na_{11}Sn_2PSe_{12}$ as the electrolyte shows excellent rate performance and a high reversible capacity of 66.2 mAh (g of TiS_2)$^{-1}$ after 100 cycles with an outstanding cycling retention of 88.3% at a rate of 0.1 C at room temperature.

Acknowledgements

Dr. Zhaoxin Yu and Dr. Shun-li Shang contributed equally to this work. The authors acknowledge financial support from the National Science Foundation (NSF) under grant DMR-1610430, and the Penn State 2017 ICS Seed Grant. First-principles calculations were carried out in part on the ACI clusters at the Pennsylvania State University, and in part on the resources of NERSC supported by the Office of Science of the U.S. Department of Energy under contract no. DE-AC02-05CH11231, and in part on the resources of XSEDE supported by NSF under grant ACI-1053575.

Appendix A. Supporting information

Structure of $Na_{11}Sn_2PSe_{12}$ for first-principles calculations; Details of first-principles, phonon, and AIMD calculations; Thermodynamic properties from first-principles and phonon calculations; Single crystal X-ray data collection, structure solution, and refinement data of $Na_{11}Sn_2PSe_{12}$; XPS profile of the surface of the $Na_{11}Sn_2PSe_{12}$ pellet before and after contact with Na metal.

Appendix A. Supplementary material

Supplementary data associated with this article can be found in the online version at doi:10.1016/j.ensm.2018.11.027.

References

[1] W. Zhou, Y. Li, S. Xin, J.B. Goodenough, Rechargeable sodium all-solid-state battery, ACS Cent. Sci. 3 (2017) 52–57. http://dx.doi.org/10.1021/acscentsci.6b00321.
[2] A. Ponrouch, E. Marchante, M. Courty, J.-M. Tarascon, M.R. Palacín, In search of an optimized electrolyte for Na-ion batteries, Energy Environ. Sci. 5 (2012) 8572–8583. http://dx.doi.org/10.1039/c2ee22258b.
[3] H. Pan, Y.-S. Hu, L. Chen, Room-temperature stationary sodium-ion batteries for large-scale electric energy storage, Energy Environ. Sci. 6 (2013) 2338–2360. http://dx.doi.org/10.1039/c3ee40847g.
[4] N. Yabuuchi, K. Kubota, M. Dahbi, S. Komaba, Research development on sodium-ion batteries, Chem. Rev. 114 (2014) 11636–11682. http://dx.doi.org/10.1021/cr500192f.
[5] X. Zheng, C. Bommier, W. Luo, L. Jiang, Y. Hao, Y. Huang, Sodium metal anodes for room-temperature sodium-ion batteries: applications, challenges and solutions, Energy Storage Mater. 16 (2019) 6–23. http://dx.doi.org/10.1016/j.ensm.2018.04.014.
[6] W. Liu, H. Zhi, X. Yu, Recent progress in phosphorus based anode materials for lithium/sodium ion batteries, Energy Storage Mater. 16 (2019) 290–322. http://dx.doi.org/10.1016/j.ensm.2018.05.020.
[7] E. Zhang, B. Wang, X. Yu, J. Zhu, L. Wang, B. Lu, β-FeOOH on carbon nanotubes as a cathode material for Na-ion batteries, Energy Storage Mater. 8 (2017) 147–152. http://dx.doi.org/10.1016/j.ensm.2017.05.012.
[8] L. Fan, Q. Liu, S. Chen, Z. Xu, B. Lu, Soft carbon as anode for high-performance sodium-based dual ion full battery, Adv. Energy Mater. (2017) 1602778. http://dx.doi.org/10.1002/aenm.201602778.
[9] Y. Kato, S. Hori, T. Saito, K. Suzuki, M. Hirayama, A. Mitsui, M. Yonemura, H. Iba, R. Kanno, High-power all-solid-state batteries using sulfide superionic conductors, Nat. Energy 1 (2016) 16030. http://dx.doi.org/10.1038/nenergy.2016.30.
[10] A. Banerjee, K.H. Park, J.W. Heo, Y.J. Nam, C.K. Moon, S.M. Oh, S.T. Hong, Y.S. Jung, Na_3SbS_4: a solution processable sodium superionic conductor for all-solid-state sodium-ion batteries, Angew. Chem. Int. Ed. 55 (2016) 9634–9638. http://dx.doi.org/10.1002/anie.201604158.
[11] K. (Kelvin), Fu, Y. Gong, J. Dai, A. Gong, X. Han, Y. Yao, C. Wang, Y. Wang, Y. Chen, C. Yan, Y. Li, E.D. Wachsman, L. Hu, Flexible, solid-state, ion-conducting membrane with 3D garnet nanofiber networks for lithium batteries, Proc. Natl. Acad. Sci. USA 113 (2016) 7094–7099. http://dx.doi.org/10.1073/pnas.1600422113.
[12] I. Villaluenga, K.H. Wujcik, W. Tong, D. Devaux, D.H.C. Wong, J.M. DeSimone, N.P. Balsara, Compliant glass-polymer hybrid single ion-conducting electrolytes for lithium batteries, Proc. Natl. Acad. Sci. USA 113 (2015) 52–57. http://dx.doi.org/10.1073/pnas.1520394112.
[13] Q. Yang, C. Li, Li metal batteries and solid state batteries benefiting from halogen-based strategies, Energy Storage Mater. 14 (2018) 100–117. http://dx.doi.org/10.1016/j.ensm.2018.02.017.
[14] B. Liu, L. Zhang, S. Xu, D.W. McOwen, Y. Gong, C. Yang, G.R. Pastel, H. Xie, K. Fu, J. Dai, C. Chen, E.D. Wachsman, L. Hu, 3D lithium metal anodes hosted in asymmetric garnet frameworks toward high energy density batteries, Energy Storage Mater. 14 (2018) 376–382. http://dx.doi.org/10.1016/j.ensm.2018.04.015.
[15] Z. Yang, J. Zhang, M.C.W. Kintner-meyer, X. Lu, D. Choi, J.P. Lemmon, Electrochemical energy storage for green grid, Chem. Rev. 111 (2011) 3577–3613. http://dx.doi.org/10.1021/cr100290v.
[16] K.B. Hueso, M. Armand, T. Rojo, High temperature sodium batteries: status, challenges and future trends, Energy Environ. Sci. 6 (2013) 734–749. http://dx.doi.org/10.1039/c3ee24086j.
[17] N. Kamaya, K. Homma, Y. Yamakawa, M. Hirayama, R. Kanno, M. Yonemura, T. Kamiyama, Y. Kato, S. Hama, K. Kawamoto, A. Mitsui, A lithium superionic conductor, Nat. Mater. 10 (2011) 682–686. http://dx.doi.org/10.1038/nmat3066.
[18] D.H. Kim, D.Y. Oh, K.H. Park, Y.E. Choi, Y.J. Nam, H.A. Lee, S.M. Lee, Y.S. Jung, Infiltration of solution-processable solid electrolytes into conventional Li-ion-battery electrodes for all-solid-state Li-ion batteries, Nano Lett. 17 (2017) 3013–3020. http://dx.doi.org/10.1021/acs.nanolett.7b00330.
[19] F. Han, T. Gao, Y. Zhu, K.J. Gaskell, C. Wang, A battery made from a single material, Adv. Mater. 27 (2015) 3473–3483. http://dx.doi.org/10.1002/adma.201500180.
[20] X. Han, Y. Gong, K. (Kelvin) Fu, X. He, G.T. Hitz, J. Dai, A. Pearse, B. Liu, H. Wang, G. Rubloff, Y. Mo, V. Thangadurai, E.D. Wachsman, L. Hu, Negating interfacial impedance in garnet-based solid-state Li metal batteries, Nat. Mater. 16 (2016) 572–579. http://dx.doi.org/10.1038/nmat4821.
[21] C. Zhang, S. Gamble, D. Ainsworth, A.M. Slawin, Y.G. Andreev, P.G. Bruce, Alkali metal crystalline polymer electrolytes, Nat. Mater. 8 (2009) 580–584. http://dx.doi.org/10.1038/nmat2474.
[22] Y.S. Jung, D.Y. Oh, Y.J. Nam, K.H. Park, Issues and challenges for bulk-type all-solid-state rechargeable lithium batteries using sulfide solid electrolytes, Isr. J. Chem. 55 (2015) 472–485. http://dx.doi.org/10.1002/ijch.201400112.
[23] S. Chen, D. Xie, G. Liu, J.P. Mwizerwa, Q. Zhang, Y. Zhao, X. Xu, X. Yao, Sulfide solid electrolytes for all-solid-state lithium batteries: structure, conductivity, stability and application, Energy Storage Mater. 14 (2018) 58–74. http://dx.doi.org/10.1016/j.ensm.2018.02.020.
[24] H. Che, S. Chen, Y. Xie, H. Wang, K. Amine, X.-Z. Liao, Z.-F. Ma, Electrolyte design strategies and research progress for room-temperature sodium-ion batteries, Energy Environ. Sci. 10 (2017) 1075–1101. http://dx.doi.org/10.1039/C7EE00524E.
[25] J.C. Bachman, S. Muy, A. Grimaud, H.-H. Chang, N. Pour, S.F. Lux, O. Paschos, F. Maglia, S. Lupart, P. Lamp, L. Giordano, Y. Shao-Horn, Inorganic solid-state electrolytes for lithium batteries: mechanisms and properties governing ion conduction, Chem. Rev. 116 (2016) 140–162. http://dx.doi.org/10.1021/acs.chemrev.5b00563.
[26] M. Ribes, B. Barrau, J. Souquet, Sulfide glasses: glass forming region, structure and ionic conduction of glasses in Na_2S-XS_2 (X = Si; Ge), Na_2S-P_2S_5 and Li_2S-GeS_2 systems, J. Non. Cryst. Solids 38–39 (1980) 271–276. http://dx.doi.org/10.1016/0022-3093(80)90430-5.
[27] A. Hayashi, K. Noi, A. Sakuda, M. Tatsumisago, Superionic glass-ceramic electrolytes for room-temperature rechargeable sodium batteries, Nat. Commun. 3 (2012) 856. http://dx.doi.org/10.1038/ncomms1843.
[28] Z. Zhu, I.-H. Chu, Z. Deng, S.P. Ong, Role of Na+ interstitials and dopants in enhancing the Na^+ conductivity of the cubic Na_3PS_4 superionic conductor, Chem. Mater. 27 (2015) 8318–8325. http://dx.doi.org/10.1021/acs.chemmater.5b03656.
[29] S. Wenzel, T. Leichtweiss, D.A. Weber, J. Sann, W.G. Zeier, J. Janek, Interfacial reactivity benchmarking of the sodium ion conductors Na_3PS_4 and sodium β-alumina for protected sodium metal anodes and sodium all-solid-state batteries, ACS Appl. Mater. Interfaces. 8 (2016) 28216–28224. http://dx.doi.org/10.1021/acsami.6b10119.
[30] N. Tanibata, M. Deguchi, A. Hayashi, M. Tatsumisago, All-solid-state Na/S batteries with a Na_3PS_4 electrolyte operating at room temperature, Chem. Mater. 29 (2017) 5232–5238. http://dx.doi.org/10.1021/acs.chemmater.7b01116.
[31] N. Tanibata, K. Noi, A. Hayashi, N. Kitamura, Y. Idemoto, M. Tatsumisago, X-ray crystal structure analysis of sodium-ion conductivity in 94 Na_3PS_4 ·6 Na_4SiS_4 glass-ceramic electrolytes, ChemElectroChem. 1 (2014) 1130–1132. http://dx.doi.org/10.1002/celc.201402016.
[32] H. Wang, Y. Chen, Z.D. Hood, G. Sahu, A.S. Pandian, J.K. Keum, K. An, C. Liang, An air-stable Na_3SbS_4 superionic conductor prepared by a rapid and economic synthetic procedure, Angew. Chem. Int. Ed. 55 (2016) 8551–8555. http://dx.doi.org/10.1002/anie.201601546.
[33] L. Zhang, K. Yang, J. Mi, L. Lu, L. Zhao, L. Wang, Y. Li, H. Zeng, Na_3PSe_4: a novel chalcogenide solid electrolyte with high ionic conductivity, Adv. Energy Mater. 5 (2015) 1501294–1501298. http://dx.doi.org/10.1002/aenm.201501294.
[34] T. Krauskopf, C. Pompe, M.A. Kraft, W.G. Zeier, Influence of lattice dynamics on Na^+ transport in the solid electrolyte $Na_3PS_{4-x}Se_x$, Chem. Mater. 29 (2017) 8859–8869. http://dx.doi.org/10.1021/acs.chemmater.7b03474.
[35] S.-H. Bo, Y. Wang, J.C. Kim, W.D. Richards, G. Ceder, Computational and experimental investigations of Na-ion conduction in cubic Na_3PSe_4, Chem. Mater. 28 (2016) 252–258. http://dx.doi.org/10.1021/acs.chemmater.5b04013.
[36] I.-H. Chu, C.S. Kompella, H. Nguyen, Z. Zhu, S. Hy, Z. Deng, Y.S. Meng, S.P. Ong, Room-temperature all-solid-state rechargeable sodium-ion batteries with a Cl-doped Na_3PS_4 superionic conductor, Sci. Rep. 6 (2016) 33733. http://dx.doi.org/10.1038/srep33733.
[37] N.J.J. De Klerk, M. Wagemaker, Diffusion mechanism of the sodium-ion solid electrolyte Na_3PS_4 and potential improvements of halogen doping, Chem. Mater. 28 (2016) 3122–3130. http://dx.doi.org/10.1021/acs.chemmater.6b00698.
[38] Z. Yu, S.-L. Shang, Y. Gao, D. Wang, X. Li, Z.-K. Liu, D. Wang, A quaternary sodium superionic conductor - $Na_{10.8}Sn_{1.9}PS_{11.8}$, Nano Energy 47 (2018) 325–330. http://dx.doi.org/10.1016/J.NANOEN.2018.01.046.
[39] L. Nazar, Z. Zhang, E. Ramos, F. Lalere, A. Assoud, K. Kaup, P. Hartmann, $Na_{11}Sn_2PS_{12}$: a new solid state sodium superionic conductor, Energy Environ. Sci.

11 (2018) 87–93. http://dx.doi.org/10.1039/C7EE03083E.
[40] J.W. Heo, A. Banerjee, K.H. Park, Y.S. Jung, S.-T. Hong, New Na-ion solid electrolytes $Na_{4-x}Sn_{1-x}Sb_xS_4$ ($0.02 \le x \le 0.33$) for all-solid-state Na-ion batteries, Adv. Energy Mater. 8 (2018) 1702716. http://dx.doi.org/10.1002/aenm.201702716.
[41] M. Duchardt, S. Neuberger, U. Ruschewitz, T. Krauskopf, W.G. Zeier, J. Schmedt auf der Günne, S. Adams, B. Roling, S. Dehnen, Superion conductor $Na_{11.1}Sn_{2.1}P_{0.9}Se_{12}$: lowering the activation barrier of Na^+ conduction in quaternary 1–4–5–6 electrolytes, Chem. Mater. 30 (2018) 4134–4139. http://dx.doi.org/10.1021/acs.chemmater.8b01656.
[42] B.J. Neudecker, W. Weppner, Li9SiAlO8: a lithium ion electrolyte for voltages above 5.4 V, J. Electrochem. Soc. 143 (1996) 2198–2203. http://dx.doi.org/10.1149/1.1836980.
[43] G. Kresse, J. Furthmüller, Efficient iterative schemes for ab initio total-energy calculations using a plane-wave basis set, Phys. Rev. B 54 (1996) 11169–11186. http://dx.doi.org/10.1103/PhysRevB.54.11169.
[44] Y. Wang, S.-L. Shang, H. Fang, Z.-K. Liu, L.-Q. Chen, First-principles calculations of lattice dynamics and thermal properties of polar solids, NPJ Comput. Mater. 2 (2016) 16006. http://dx.doi.org/10.1038/npjcompumats.2016.6.
[45] S.L. Shang, Y. Wang, D. Kim, Z.K. Liu, First-principles thermodynamics from phonon and Debye model: application to Ni and Ni_3Al, Comput. Mater. Sci. 47 (2010) 1040–1048. http://dx.doi.org/10.1016/j.commatsci.2009.12.006.
[46] P. Bron, S. Johansson, K. Zick, J. Schmedt, D. Günne, S.S. Dehnen, B. Roling, $Li_{10}SnP_2S_{12}$ - an affordable lithium superionic conductor, J. Am. Chem. Soc. 135 (2013) 15694–15697. http://dx.doi.org/10.1021/ja407393y.
[47] Z. Yu, S.-L. Shang, J.-H. Seo, D. Wang, X. Luo, Q. Huang, S. Chen, J. Lu, X. Li, Z.-K. Liu, D. Wang, Exceptionally high ionic conductivity in $Na_3P_{0.62}As_{0.38}S_4$ with improved moisture stability for solid-state sodium-ion batteries, Adv. Mater. 29 (2017) 1605561. http://dx.doi.org/10.1002/adma.201605561.
[48] J.W. Hoe, A. Banerjee, K.H. Park, Y.S. Jung, S.T. Hong, New Na-ion solid electrolytes $Na_{4-x}Sn_{1-x}Sb_xS_4$ ($0.02 \le x \le 0.33$) for all-solid-state Na-ion batteries, Adv. Energy Mater. (2018) 1702716. http://dx.doi.org/10.1002/aenm.201702716.
[49] O. Bohnke, S. Ronchetti, D. Mazza, Conductivity measurements on nasicon and nasicon-modified materials, Solid State Ion. 122 (1999) 127–136. http://dx.doi.org/10.1016/S0167-2738(99)00062-4.
[50] M. Duchardt, U. Ruschewitz, S. Adams, S. Dehnen, B. Roling, Vacancy-controlled Na^+ superion conduction in $Na_{11}Sn_2PS_{12}$, Angew. Chem. Int. Ed. 130 (2018) 1365–1369. http://dx.doi.org/10.1002/anie.201712769.
[51] W. Xue, Y. Yang, Q. Yang, Y. Liu, L. Wang, C. Chen, R. Cheng, The effect of sintering process on lithium ionic conductivity of $Li_{6.4}Al_{0.2}La_3Zr_2O_{12}$ garnet produced by solid-state synthesis, RSC Adv. 8 (2018) 13083–13088. http://dx.doi.org/10.1039/c8ra01329b.
[52] K.H. Park, Q. Bai, D.H. Kim, D.Y. Oh, Y. Zhu, Y. Mo, Y.S. Jung, Design strategies, practical considerations, and new solution processes of sulfide solid electrolytes for all-solid-state batteries, Adv. Energy Mater. 8 (2018) 1–24. http://dx.doi.org/10.1002/aenm.201800035.
[53] C.K. Moon, H.J. Lee, K.H. Park, H. Kwak, J.W. Heo, K. Choi, H. Yang, M.S. Kim, S.T. Hong, J.H. Lee, Y.S. Jung, Vacancy-driven Na+ superionic conduction in new Ca-doped Na_3PS_4 for all-solid-state Na-ion batteries, ACS Energy Lett. 3 (2018) 2504–2512. http://dx.doi.org/10.1021/acsenergylett.8b01479.
[54] S.L. Shang, L.G. Hector Jr, Y. Wang, H. Zhang, Z.K. Liu, First-principles study of elastic and phonon properties of the heavy fermion compound CeMg, J. Phys. Condens. Matter. 21 (2009) 246001. http://dx.doi.org/10.1088/0953–8984/21/24/246001.
[55] S.L. Shang, Y. Wang, P.W. Guan, W.Y. Wang, H.Z. Fang, T. Anderson, Z.-K. Liu, Insight into structural, elastic, phonon, and thermodynamic properties of alpha-sulfur and energy-related sulfides: a comprehensive first-principles study, J. Mater. Chem. A 3 (2015) 8002–8014. http://dx.doi.org/10.1039/c4ta07062c.
[56] S.L. Shang, Y. Wang, B. Gleeson, Z.-K. Liu, Understanding slow-growing alumina scale mediated by reactive elements: perspective via local metal-oxygen bonding strength, Scr. Mater. 150 (2018) 139–142. http://dx.doi.org/10.1016/j.scriptamat.2018.03.002.
[57] Z. Liu, Y. Tang, Y. Wang, F. Huang, High performance $Li_2S–P_2S_5$ solid electrolyte induced by selenide, J. Power Sources 260 (2014) 264–267. http://dx.doi.org/10.1016/j.jpowsour.2014.03.036.
[58] J. Kim, Y. Yoon, M. Eom, D. Shin, Characterization of amorphous and crystalline $Li_2S–P_2S_5–P_2Se_5$ solid electrolytes for all-solid-state lithium ion batteries, Solid State Ion. 225 (2012) 626–630. http://dx.doi.org/10.1016/j.ssi.2012.05.013.
[59] G. Adam, J.H. Gibbs, On the temperature dependence of cooperative relaxation properties in glass-forming liquids, J. Chem. Phys. 43 (1965) 139–146. http://dx.doi.org/10.1063/1.1696442.
[60] I. Saika-Voivod, P.H. Poole, F. Sciortino, Fragile-to-strong transition and polyamorphism in the energy landscape of liquid silica, Nature 412 (2001) 514–517. http://dx.doi.org/10.1038/35087524.